Mineralium Deposita (2020) 55:1407–1424
https://doi.org/10.1007/s00126-019-00948-7

ARTICLE

Geology, geochronology, and S-Pb-Os geochemistry of the Alastuo gold deposit, West Tianshan, NW China

Bo Zu[1] · Chunji Xue[2] · Reimar Seltmann[3] · Alla Dolgopolova[3] · Guoxiang Chi[4] · Chao Li[5]

Received: 21 January 2019 / Accepted: 2 December 2019 / Published online: 6 January 2020

Abstract

The Alastuo gold deposit, located in the Narati region of the Chinese West Tianshan, is a newly discovered gold deposit within the world-class Tianshan gold belt. The gold mineralization is hosted by an Early Carboniferous granodiorite intrusion and controlled structurally by subsidiary faults of the transcrustal North Narati Fault. The deposit consists of auriferous alteration assemblages and minor vein ores. Field relations and petrographic data suggest four stages of mineralization with gold precipitated coevally with quartz, chlorite, epidote, pyrite, and galena during the second and third stages that are characterized by tectonic transformation from ductile shearing to brittle deformation. The temperature range of gold precipitation is estimated to be 280–330 °C using chlorite geothermometry. Ten auriferous pyrite samples yielded a well-defined Re-Os isochron age of 325 ± 3 Ma and two sericite samples yielded plateau-like $^{40}Ar/^{39}Ar$ ages of 321.7 ± 3.0 Ma and 321.2 ± 2.8 Ma. These consistent ages suggest that the gold mineralization in the Narati region was emplaced in a transitional regime from subduction to continental collision between the Tarim block and Middle Tianshan terrane (325–310 Ma), rather than during the post-collisional stage as in most part of the Tianshan gold belt. Gold-bearing pyrite has an initial Os_i value of 0.7 ± 0.1 and lead isotopes ratios of 17.897 to 18.723 for $^{206}Pb/^{204}Pb$, 15.474 to 15.643 for $^{207}Pb/^{204}Pb$, and 37.522 to 38.299 for $^{208}Pb/^{204}Pb$, while samples of pyrite, galena, and sphalerite have $^{34}S_{V\text{-}CDT}$ of +1.9 to +7.8‰. The isotope data suggest that the sulfur and metals are most likely derived from mixed mantle and crustal sources including metamorphic devolatilization of subducted oceanic slab and overlying sedimentary rocks. The mineralization styles, structural controls, metal and sulfur sources, and the timing of gold mineralization with respect to the orogenic event all suggest that the Alastuo gold deposit represents an orogenic type deposit. This newly recognized Carboniferous orogenic gold mineralization event calls for a re-evaluation of the gold metallogeny in the Middle Tianshan.

Keywords Alastuo gold deposit · Granitoid-hosted mineral system · Orogenic gold mineralization · Tianshan gold belt · Re-Os geochronology · $^{40}Ar/^{39}Ar$ geochronology · Os-S-Pb fingerprinting

Editorial handling: H. Chen

Electronic supplementary material The online version of this article (https://doi.org/10.1007/s00126-019-00948-7) contains supplementary material, which is available to authorized users.

✉ Chunji Xue
chunji.xue@cugb.edu.cn

[1] School of Earth Resources, China University of Geosciences, Wuhan 430074, China

[2] State Key Laboratory of Geological Processes and Mineral Resources, School of Earth Sciences and Resources, China University of Geosciences, Beijing 100083, China

[3] Department of Earth Sciences, Natural History Museum, Center for Russian and Central EurAsian Mineral Studies, Cromwell Road, London SW7 5BD, UK

[4] Department of Geology, University of Regina, Regina, Saskatchewan S4S 0A2, Canada

[5] National Research Center for Geoanalysis, Beijing 100037, China

Introduction

The Central Asian Orogenic Belt (CAOB) is the world's largest Phanerozoic orogenic belt (e.g., Jahn 2004) and it is endowed with numerous large gold deposits forming several world-class gold provinces (Yakubchuk et al. 2005). The Tianshan gold belt on the southwestern margin of the CAOB (Fig. 1a) stretches over 2500 km along an E-W axis from western Uzbekistan to Xinjiang in NW China (e.g., Sengör et al. 1993; Xiao et al. 2015). This belt is the richest gold province in the CAOB (Yakubchuk et al. 2002, 2005), encompassing the world-class Muruntau and Kumtor deposits. Numerous gold deposits are located mostly in the western part of the South and Middle Tianshan including those in Uzbekistan, Tajikistan, and Kyrgyzstan that have been extensively described (e.g., Kudrin et al. 1990; Cole et al. 2000; Mao et al. 2004). Available data suggest a prolonged history of gold mineralization covering a major part of the late Paleozoic with gold ore formation being associated with subduction or collision-related metamorphism and/or magmatism (e.g., Cole et al. 2000; Abzalov 2007; Kempe et al. 2016; Soloviev et al. 2018).

Many comparative studies indicate that the Tianshan gold belt is a continuous geological terrane that extends eastward into the Chinese Tianshan (e.g., Chen 2000; Rui et al. 2002; Zhu et al. 2007; Pirajno et al. 2011); however, the number and size of the discovered Au deposits in China's segment of the Tianshan are much less important (e.g., Liu et al. 2007; Chen et al. 2008; Xue et al. 2014; Chen et al. 2012). Recent exploration activities have led to some significant discoveries in the Chinese Tianshan, including the Kateba'su (76 t Au @ 3.84 g/t) and the smaller satellite Niyazitiekexie and Alastuo gold deposits in the Narati region (Fig. 1c; Yang et al. 2013; Xue et al. 2014; Zhang et al. 2015). These three deposits are all hosted by Late Paleozoic granitic intrusions and controlled by subsidiary faults and fractures zones near the major North

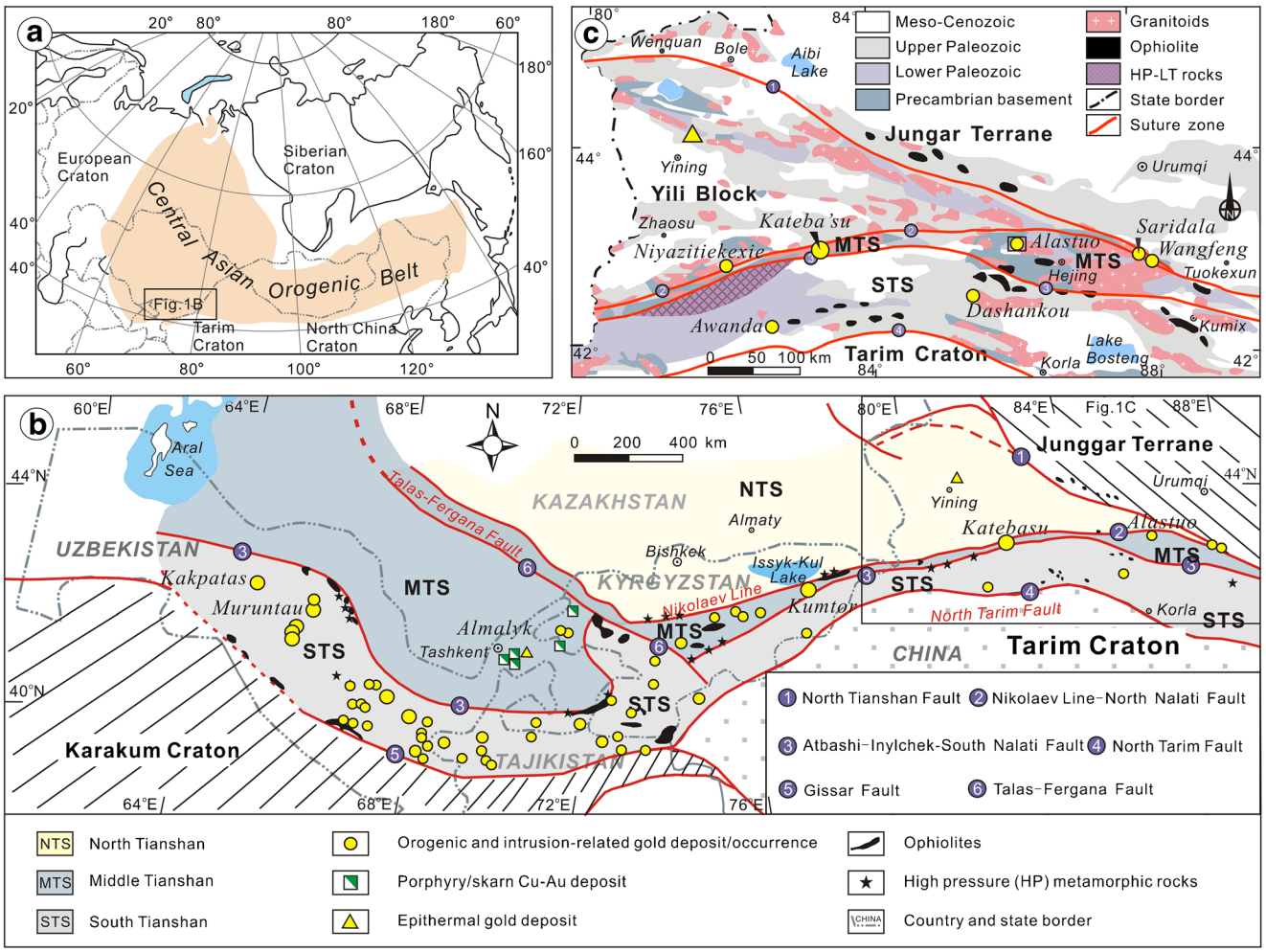

Fig. 1 (**a**) Tectonic location of the Tianshan metallogenic belt in the Central Asian Orogenic Belt. (**b**) Principal tectonic zones and lineaments of the Tianshan orogenic belt showing the distribution of ophiolites, high-pressure low-temperature rocks (HPLT) and major Au deposits (modified after Soloviev et al. 2018, Xue et al. 2014 and Yakubchuk et al. 2005). (**c**) Geological map of the Chinese Tianshan and location of the Alastuo gold deposit in the Narati region (modified after Gao et al. 2009 and Xu et al. 2013)

Narati Fault (NNF) (Yang et al. 2013; Zhang et al. 2015; Zhao et al. 2019). However, the precise age and genesis of these newly discovered deposits remain poorly understood. For example, the Kateba'su, largest gold deposit in the Narati region, has a garnet Sm-Nd isochron age of 334 Ma (Liu et al. 2018), a pyrite Rb-Sr isochron age of 323 Ma (Dong et al. 2018), a pyrite Re-Os isochron age of 311 Ma (Zhang et al. 2015), and a sericite $^{49}Ar/^{39}Ar$ age of 269 Ma (Gao et al. 2015). The genesis of the gold deposits in the Narati region has been deemed previously to be either of orogenic-type or porphyry-type based mainly on research of the Kateba'su gold deposit (Yang et al. 2013; Zhang et al. 2015; Dong et al. 2018; Liu et al. 2018). To date, little has been known about the geochronology and genesis of the Alastuo gold deposit, as well as its possible relations with the Kateba'su gold deposit in the same region or with other gold deposits in the Tianshan gold belt.

The Alastuo Au deposit at the easternmost end of the Narati region was recently discovered during regional reconnaissance exploration by the First Brigade of Regional Geological Survey of the Xinjiang Bureau of Geology and Mineral Resources (Bahebatuo Mining Company 2015). Although only 9.4 t of gold has been delineated so far by trenching and initial drilling, a total resource of more than 100 t Au is indicated for the area in a recent mineral resource assessment (Bahebatuo Mining Company 2015; Zu 2016). The Alastuo gold deposit has many similarities to the larger Kateba'su gold deposit and thus it may provide new evidence on the genesis of the gold-bearing mineral systems in the Narati region. In this paper, we present an integrated geological, geochronological and isotopic study of the Alastuo gold deposit, aiming to provide constraints on the nature, age, source, and the genesis of gold mineralization. In a wider context, the comparison of Alastuo to the regional metallogeny may reveal more about the potential for further Au exploration in the Narati region.

Geological setting

Regional tectonic framework

The Tianshan belt is an orogenic collage that formed during several Paleozoic accretion-collision events related to the progressive closure of the Paleo-Asian Ocean (Gao et al. 2009; Biske et al. 2013; Xiao et al. 2013). The tectonic framework of the Tianshan orogenic belt is subdivided traditionally into three structurally bounded tectonic units, which are named, from north to south, the North, Middle, and South Tianshan (Fig. 1b) (Charvet et al. 2011; Gao et al. 2009).

The North Tianshan unit includes the North Tianshan Accretionary Complex (NTAC), Kazakhstan-Yili Block (KYB) and Kyrgyzstan North Tianshan (KNT) that are separated from the Middle Tianshan unit by the Nikolaev Line in Kyrgyzstan and the North Narati fault (NNF) in China (Charvet et al. 2011). The NTAC is composed mainly of Late Carboniferous volcano-sedimentary rocks and ophiolitic slices left from the consumption of the North Tianshan Ocean (Wang et al. 2006). To the south, the KYB is composed of Precambrian basement that is overlain by early to late Paleozoic clastic sedimentary and volcano-sedimentary rocks. To the southwest, the KNT is considered to be an early Paleozoic magmatic arc that was formed by the progressive northward subduction of the Terskey Ocean in the Late Ordovician (Konopelko et al. 2008).

The Middle Tianshan unit is a narrow continental massif located between the Nikolaev Line-North Narati Suture Zone and the Atbashi-Inylchek-South Narati Fault Zone (Fig. 1c) (Alexeiev et al. 2016). The unit includes the Chinese Middle Tianshan and the Kyrgyz Middle Tianshan, and it is considered to be a continental fragment that rifted off the Tarim block during either the Neoproterozoic or Paleozoic (Ma et al. 2014). The Chinese Middle Tianshan is characterized by Precambrian basement rocks, Ordovician to Early Devonian magmatic arc volcanic and sedimentary sequences, and undeformed Late Paleozoic sedimentary cover (Ma et al. 2014; Zhong et al. 2017; He et al. 2018). Voluminous Paleozoic granitoids in the Middle Tianshan have yielded Early Paleozoic to Early Permian ages (500–260 Ma) and record multiple stages of subduction, collision and post-collisional events (Xu et al. 2013; Zhang et al. 2017; Zhong et al. 2017).

Abutting the Middle Tianshan, the South Tianshan Accretionary Complex represents a wide zone between the Atbashi-Inylchek-South Narati Fault and the Northern Tarim Margin Fault (Fig. 1c) (Gao et al. 2009; Wang et al. 2017; Xiao et al. 2013). The Atbashi-Inylchek-South Narati Fault is characterized by several separate mid- to late-Paleozoic ophiolitic mélanges and high-pressure (HP) metamorphic terranes (Akyazi and Atbashi) with peak metamorphism at ~ 325–310 Ma (Hegner et al. 2010; Gao et al. 2011; Zhang et al. 2013; Klemd et al. 2015). The main body of the accretionary complex is composed of imbricated Late Ordovician-Carboniferous clastic sedimentary rocks and limestone that are uncomfortably overlain by Permian fluvial deposits and rift-type volcanic rocks (Jiang et al. 2014). Voluminous Early Permian (304–270 Ma) A-type granites are interpreted to record a regional large-scale post-collisional extension after the final amalgamation of the Tarim and Kazakhstan blocks (Huang et al. 2015a; Dolgopolova et al. 2017).

The Tianshan gold belt is primarily noted for its rich endowment of multiple types of gold deposits, including orogenic to reduced intrusion-related Au (e.g., Kudrin et al. 1990; Mao et al. 2004; Abzalov 2007; Chen et al. 2012a), large porphyry-skarn Au-Cu (e.g., Seltmann et al. 2014; Soloviev et al. 2018; Zu et al. 2019) and epithermal Au-Ag deposits (e.g., Chen et al. 2012b; Seltmann et al. 2014). The total gold

endowment of this belt and its neighboring terrains may exceed 400 Moz (Yakubchuk et al. 2002). These deposits were formed mainly during the Late Paleozoic Hercynian orogeny due to subduction/collision-related magmatism, metamorphism, and continental margin deformation (e.g., Seltmann et al. 2011). Gold mineralization is associated with major transcrustal shear zones that provided a primary focus for deformation, regional fluid flow, and ore precipitation (e.g., Cole et al. 2000).

Geology of the Narati region

The Alastuo gold deposit is located at the eastern side of the Narati region of the Chinese Middle Tianshan (Fig. 1c). The Narati region is sandwiched between the North and South Narati Faults (NNF and SNF, respectively) and occurs as a narrow zone from Southern Zhaosu in the west to Western Hejing in the east. The basement of the Narati region is mainly composed of greenschist- to amphibolite-facies and locally granulite-facies metasedimentary rocks with associated volcanic rocks and intrusions, including migmatites, orthogneisses, amphibolites, crystalline schists, and marbles of Paleo- to Neoproterozoic ages (Huang et al. 2015b; Wang et al. 2017). The basement is unconformably overlain by the Silurian Bayinbuluk Formation with thick andesite volcanic rocks and tuffs above sandstone and limestone. The volcanic rocks are also closely associated with widespread early Paleozoic intrusions that formed in an arc setting (He et al. 2018). The Late Carboniferous volcanic and sedimentary rocks are mainly distributed in the Yili block to the north of the NNF (Fig. 1c).

The structural framework in the Narati region is characterized by the EW-trending NNF, SNF, and their subsidiary faults (Fig. 1c). The NNF occurs as a series of reverse faults dipping south at various angles (mostly ~ 60°) (Yang et al. 2013). This fault is inferred to be inherited from the paleolocation of the subduction suture zone of the early Paleozoic Terskey Ocean and reactivated as strike-slip faults during its Late Paleozoic tectonic evolution (Charvet et al. 2011). The SNF contains discontinuous ophiolitic mélanges and high-pressure metamorphic terranes, which are interpreted to represent the suture zone of the South Tianshan Ocean that closed at the end of the Carboniferous (Gao et al. 2011; Xiao et al. 2013). The Alastuo and Kateba'su gold deposits are spatially close to the NNF and its subsidiary faults (Fig. 1c) (Zhao et al. 2019).

Granitic rocks are widely distributed in the Narati region (Fig. 1c). Early Ordovician magmatism is characterized by intermediate-basic intrusions with calc-alkaline affinity that were formed during the closure of the Terskey Ocean and the incipient opening of the south Tianshan back-arc basin (Gao et al. 2009; Zhang et al. 2017). Silurian magmatism is related to the initial subduction of the South Tianshan oceanic crust, resulting in volcano-plutonic calc-alkaline arc formations (Zhong et al. 2017). The arc magmatism culminated during the Late Devonian to Early Carboniferous (~ 345 to 320 Ma), which is interpreted to be the major stage of subduction (Xu et al. 2013; Zhang et al. 2017). The Late Carboniferous period is the most important transitional time for the Tianshan orogenic belt, which corresponds to the transition from convergence to a post-collisional tectonic environment (Long et al. 2011). The Permian magmatism (~ 300–270 Ma) took place during the post-collisional process and exhibits alkali-calcic to alkali compositions (Long et al. 2011; Ma et al. 2014). For the gold deposits, the Late Devonian to Early Carboniferous magmatic rocks are the most important hosts, including for Kateba'su and Alastuo (Dong et al. 2018; Han et al. 2018).

Geology of the Alastuo gold deposit

The Alastuo gold deposit is located in the eastern part of the Narati region and near the south margin of the NNF (Fig. 1c). The sedimentary sequence in the deposit area consists mainly of sandstone, siltstone, and limestone of the Lower Silurian Bayinbuluke Formation, which is intruded by the Late Paleozoic Abuduerqiaolun complex (Fig. 2). The complex is composed of granodiorite, monzogranite, and granite with crosscutting dykes of diorite porphyry, granite porphyry, and diabase. Minor Precambrian schist and gneiss blocks occur locally as xenoliths in the granodiorite of the Abuduerqiaolun complex (Bahebatuo Mining Company 2015). The granodiorite has a zircon U-Pb age of 350.3 ± 3.0 Ma (Han et al. 2018).

Gold orebodies (> 1.0 g/t) and Au mineralized bodies (> 0.3 g/t) are hosted mainly in the granodiorite and monzogranite phases of the Abuduerqiaolun complex (Fig. 3a, b). Sixteen orebodies have been delineated to date in the Alastuo gold deposit (Bahebatuo Mining Company 2015). These orebodies occur mainly in the granodiorite intrusion along subparallel NNE-trending subsidiary ductile to brittle faults and mylonites (Fig. 2a). Ductile deformation fabrics, such as the elongated deformation and recrystallization of quartz (Fig. 4a), are developed in the mylonite zones. The orebodies are lenticular and extend up to 500 m along strike, 50 to 250 m in thickness (Fig. 2a), and dip steeply 55 to 80° to the southeast, but their depth extension has not yet been well constrained (Fig. 2b).

Based on their mineral association and ore structure, two major types of mineralization have been identified in the Alastuo deposit, namely, the sulfide-quartz vein-type and the altered-rock type, with the latter being more important (Bahebatuo Mining Company 2015). The sulfide-quartz vein-type orebodies occur along the subsidiary faults with widths of tens of centimeters to several meters. The altered-rock ores are also controlled by faults and mylonite zones, and

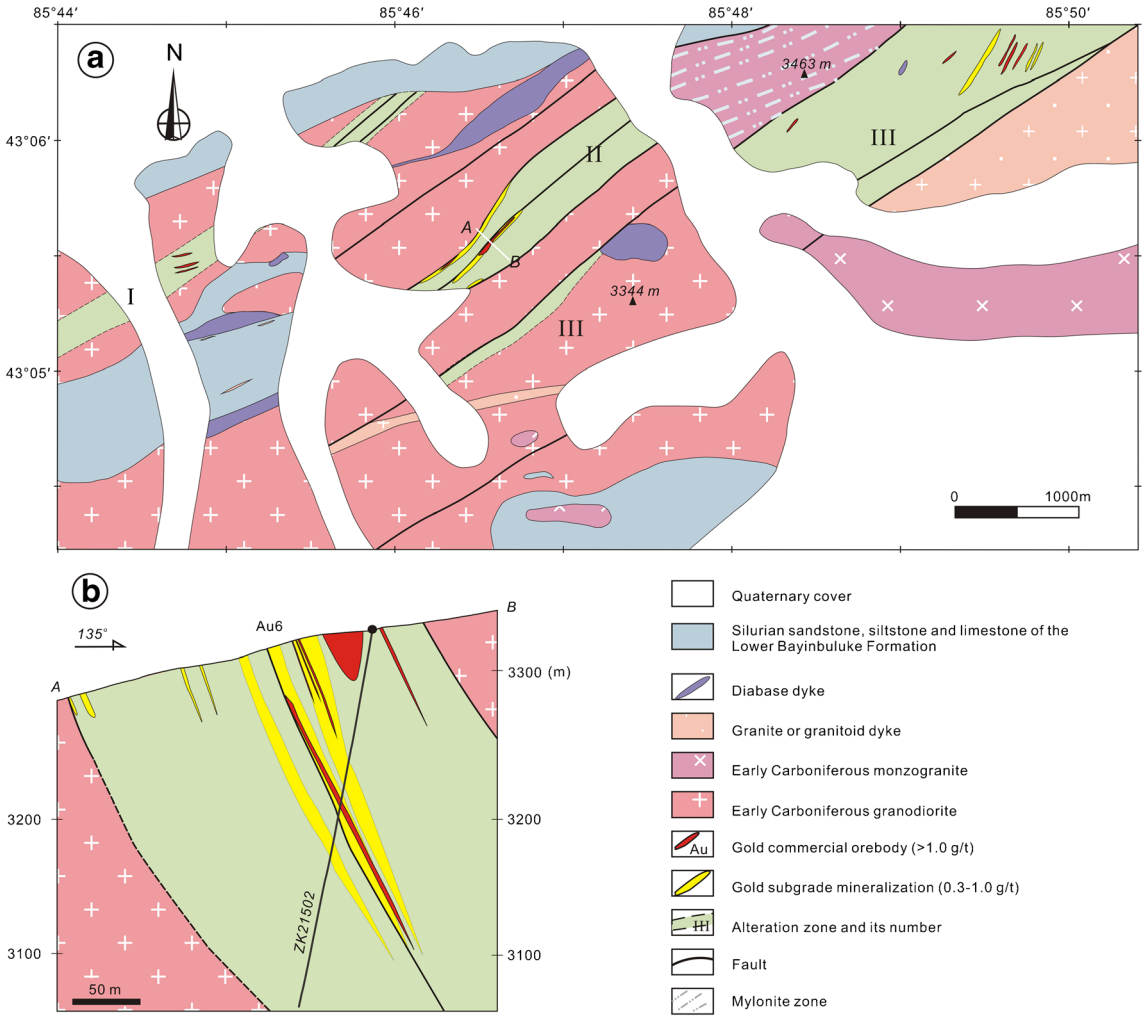

Fig. 2 Simplified geologic map (**a**) and cross section (**b**) of the Alastuo gold deposit (modified after Bahebatuo Mining Company 2015)

they are characterized by a pyrite + quartz + chlorite + sericite assemblage (Fig. 3f–h). The metallic minerals are dominantly pyrite (> 90 vol%), with subordinate galena, pyrrhotite, sphalerite, chalcopyrite, and arsenopyrite (Fig. 4d–i). Gold occurs as native gold (91.6 wt% to 93.6 wt% Au) with high Au/Ag ratios that that range from 14.0 to 17.7 (ESM 3). Native gold grains occur mainly in gangue minerals (Fig. 4d–f) with an especially close relationship to chlorite veins (Fig. 4d, e). Minor gold grains are found beside pyrite and galena crystals or as inclusions in pyrite (Fig. 4g, h; ESM Fig. 1). A rare argentite grain was identified by electron microprobe analysis (EMPA) with about 86 wt% Ag.

Hydrothermal alteration of wallrocks in the Alastuo deposit includes silicification, sericitization, chloritization, epidotization, carbonatization, fluoritization, and sulfidation (Figs. 3 and 4). Silicification is mainly developed around the quartz veins (Fig. 3d) and is associated with euhedral to subhedral pyrite (Fig. 3c–e) and minor sericite (Figs. 3e, 4a). Sericitization is pervasive throughout the alteration zones, and occurs as disseminations with sulfides, hydrothermal quartz and chlorite (Fig. 3e–g, 4a–b). Chlorite generally occurs as the replacement of pre-existing biotite or amphibole, but it also occurs as veins or veinlets, especially in high-grade ore zones (Fig. 3f–h). One of the highest-grade samples (sample A96; Fig. 3h; ESM 2) revealed an intimate relationship between chlorite and gold along fractures in a quartz vein (Fig. 4d–f). Epidote is locally developed and occurs with chlorite, quartz and pyrite in veins (Fig. 3f, 4c). Actinolite occurs as aggregates dispersed among other alteration minerals, and fluorite, commonly associated with calcite, is disseminated in the altered rocks.

Mineralogical, textural, and field relationships delineate four stages of alteration and mineralization in the Alastuo gold deposit (Fig. 5). Stage I is represented by quartz veins and pervasively distributed silicification (Fig. 4a–c) with minor pyrite and sericite (Figs. 3c, 4a). Importantly, some of the quartz is locally deformed due to ductile deformation (Fig. 4a), implying a close spatial and temporal relationship

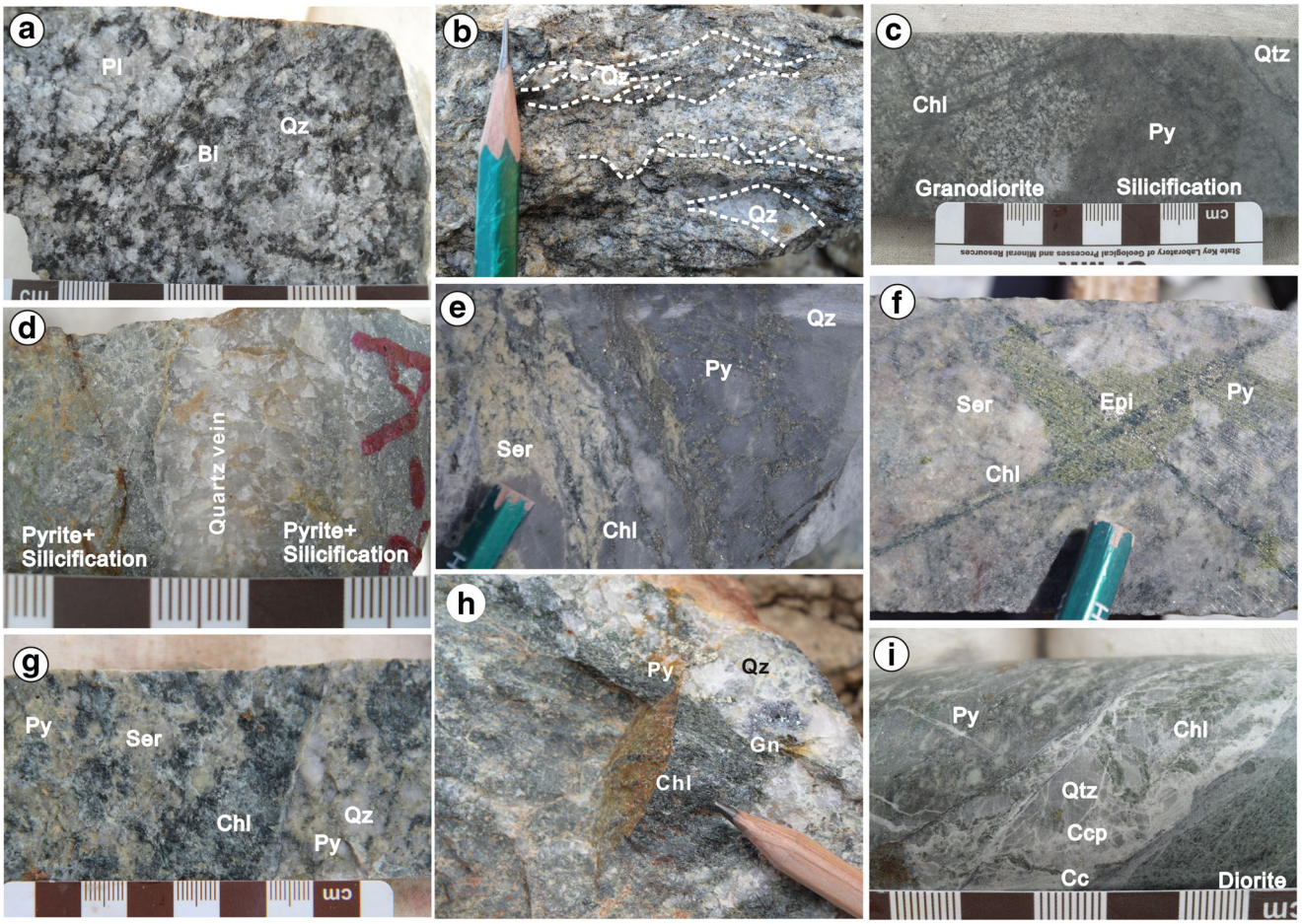

Fig. 3 Photographs showing the primary wallrocks and ores with various alteration styles. (**a**) Granodiorite (the main host for the orebodies), note the weak orientation alignment of biotite; (**b**) Mylonitized granitoid with strongly deformed quartz and plagioclase; (**c**) Strong silicification overprinting granodiorite with minor disseminated pyrite; (**d**) Transitional change from clear quartz veins to nearby silicification and associated pyrite; (**e**) Quartz-pyrite veins replacing sericitized granitoids with fine chlorite veins along fractures; (**f**) Granitoid crosscut by epidote and later chlorite-pyrite veins; (**g**) Altered granitoids with sericite and chlorite alterations and disseminated pyrite; (**h**) Altered granitoids with chlorite, quartz, pyrite, and galena; and (**i**) Altered diorite crosscut by quartz, chlorite, calcite, and chalcopyrite veins along fractures. Cc, calcite; Chl, chlorite; C, chalcopyrite; Epi, epidote; Fl, fluorite; Py, pyrite; Qz, quartz; Ser, sericite

with the deformation zones. Stage II (sulfide-quartz stage) is characterized by pyrite-quartz veins and veinlets (Fig. 3d–e), accompanied by minor silicification and sericitization (Fig. 3e). This is one of the ore-forming stages, with local development of high-grade ores (Bahebatuo Mining Company 2015), as reflected by native gold in fractures of a cubic pyrite crystal (ESM Fig. 1). Stage III (polymetallic sulfide-quartz-chlorite stage) is characterized by extensive chloritization, sericitization, epidotization, and sulfidation (Fig. 3f–h). This is the most important ore-forming stage as it yields abundant native gold (Fig. 4e–h). The sulfides are mainly pyrite, sphalerite, and galena with minor arsenopyrite, pyrrhotite, chalcopyrite, and argentite (Fig. 4g–i). Stage IV is characterized by quartz-calcite veins with sparsely distributed pyrite, chalcopyrite, and fluorite (Fig. 3i). This is the waning stage of the hydrothermal system and has little or no gold mineralization.

Sampling and analytical methods

Pyrite Re-Os dating

Pyrite separates of 10 samples from the sulfide-quartz stage (stage II) (ESM 2) were produced via rough crushing and subsequent handpicking of pyrite grains of approximately 40–60 mesh-size fractions. For Re-Os geochronology, all chemical procedures and analytical methods were performed at the National Research Center of Geoanalysis, Chinese Academy of Geological Sciences (CAGS), following Du et al. (2012) and references therein. In brief, about 0.70 g of pyrite were loaded into a Carius tube with spikes of ^{185}Re and ^{190}Os and dissolved in a reverse aqua regia solution. Osmium was separated by distillation and purified using a microdistillation technique. Re was extracted by acetone and further repurified using a cation exchange column. Re and Os compositions and their

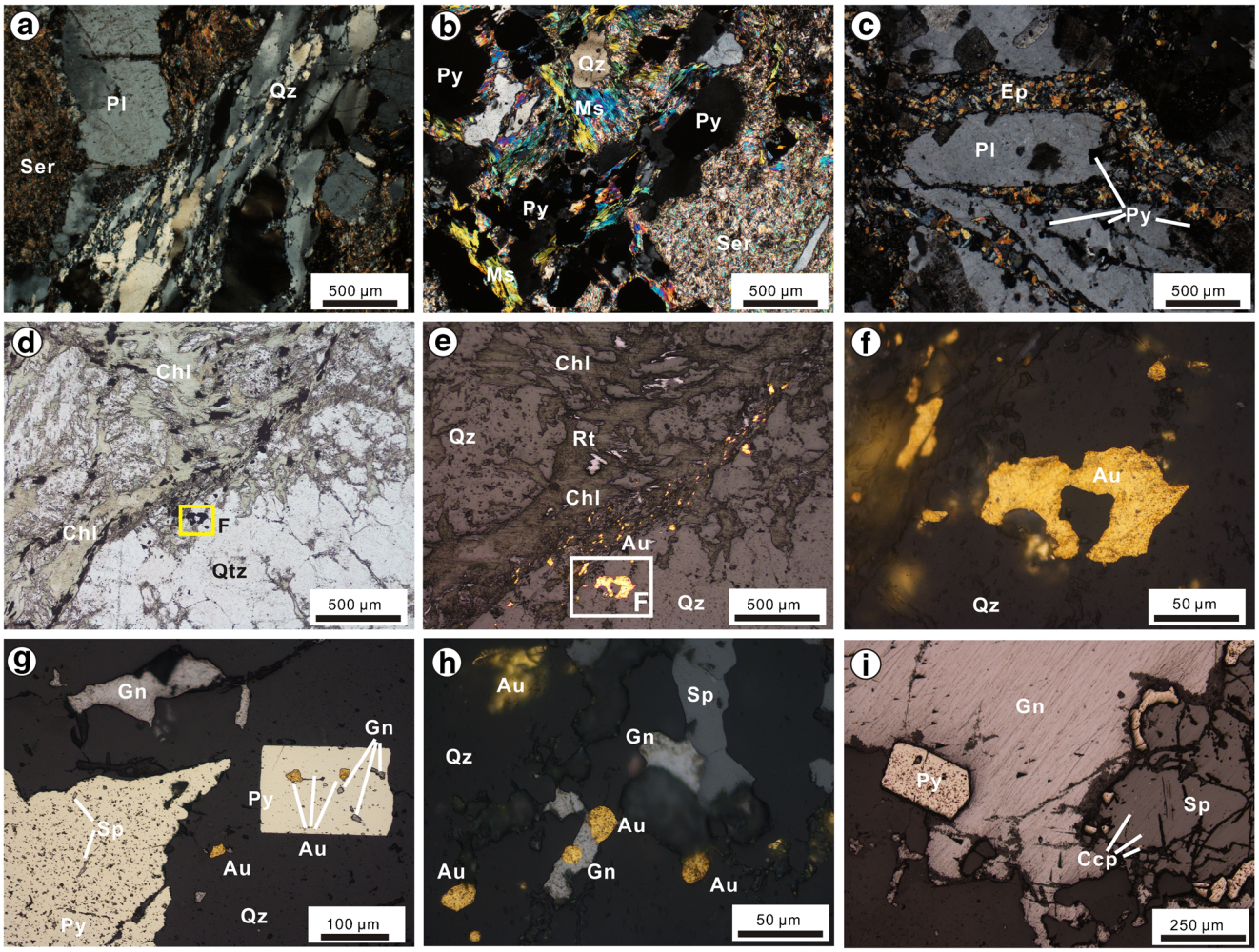

Fig. 4 Photomicrographs showing the principal alteration associations and gold occurrences; (**a**) Mylonite composed of deformed quartz and sericite, with quartz showing elongated deformation and recrystallization; (**b**) Alteration assemblage composed of quartz, sericite and pyrite typical of the Alastuo deposit; (**c**) Plagioclase crosscut by epidote-pyrite veins; (**d**–**f**) A gold-rich sample with native gold occurring with quartz and chlorite. Note the trail of gold grains along the chlorite veins (**d**, **e**); (**g**) Gold occurring as inclusions in pyrite or as free gold in quartz; (**h**) Gold occurring as ovate grains coexisting with galena or as free gold in quartz; (**i**) The coexistence of pyrite, galena, and sphalerite in the quartz-polymetallic stage. Au, native gold; Chl, chlorite; Ccp, chalcopyrite; Ep, epidote; Gn, galena; Ms., muscovite; Pl, plagioclase; Py, pyrite; Qz, quartz; Rt, rutile; Ser, sericite; Sp, sphalerite

isotopic ratios were determined using a Finnigan Triton N-TIMS instrument with an in-house monitor sample JCBY (Qu et al. 2009). Procedure blanks are 0.0012 ng/g for Re and 0.0001 ng/g for common Os, which are significantly lower than the Re and Os concentrations in the analyzed samples (ESM 4). The tests of the JCBY standard sample analyzed during this study yielded 38.690 ng/g for Re, 16.259 ng/g for Os and 0.3344 ± 0.0005 for $^{187}Os/^{188}Os$, which are consistent with the recommended values (38.61 ± 0.53 ng/g for Re, 16.23 ± 0.17 ng/g for Os and 0.3363 ± 0.0029 for $^{187}Os/^{188}Os$) (Qu et al. 2009).

Sericite $^{40}Ar/^{39}Ar$ dating

Two sericite samples (A16 and A18) were separated from high-grade Au ores of the polymetallic sulfide-quartz-chlorite-sericite stage (stage III) for $^{40}Ar/^{39}Ar$ dating (ESM 2). The sericite is well crystallized and has a close textural relationship with pyrite (Fig. 4b). The samples were crushed to minus-20-mesh, from which mica flakes were separated using conventional heavy liquid and magnetic techniques and then cleaned by ultrasonic bath. Sericite separates of high purity were then handpicked under a binocular microscope.

The samples and a monitoring standard (ZBH-25: 132.7 ± 1.2 Ma; Wang 1983) were irradiated for 55 h in a Swimming Pool Reactor at the China Institution of Atomic Energy in Beijing. After a 3-month cooling period, the samples were analyzed by the $^{40}Ar/^{39}Ar$ incremental heating method using a Helix MC mass spectrometer at the Key Laboratory of Isotope Geology, CAGS,

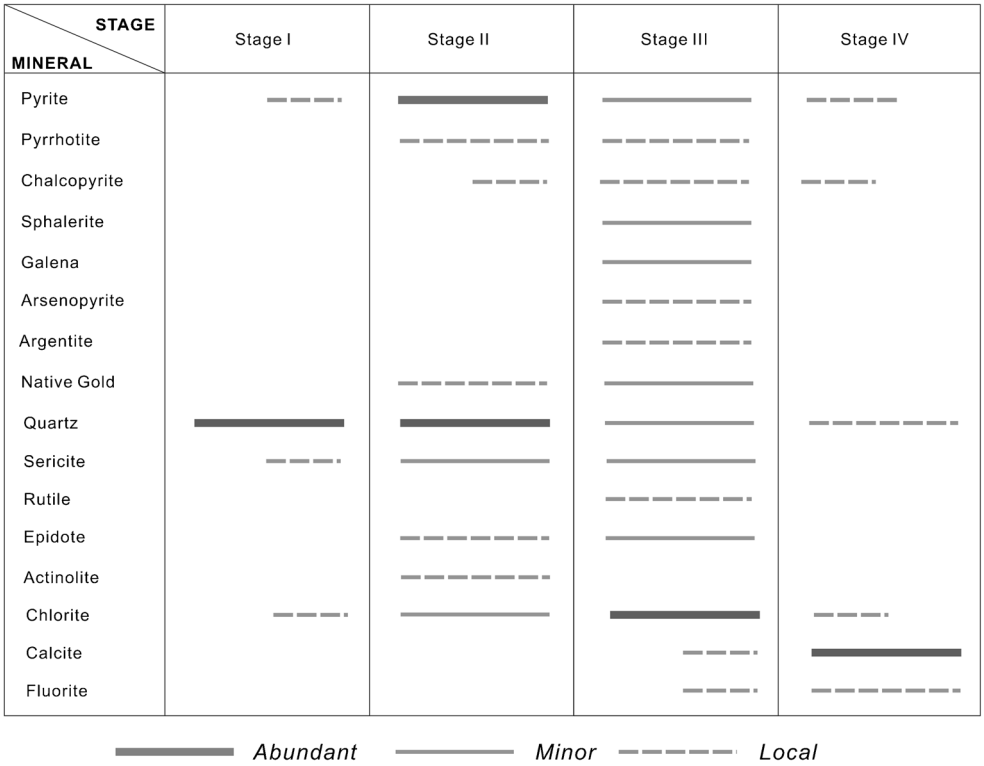

Fig. 5 Paragenetic sequence for the Alastuo gold deposit

Beijing, following the analytical procedures described by Chen et al. (2002). All ages were calculated using 5.543×10^{-10} a^{-1} as the total decay constant for ^{40}K (Steiger and Jäger 1977), and the values for the reactor correction factors are 8.06×10^{-4} for $(^{39}Ar/^{37}Ar)_{Ca}$, 2.40×10^{-4} for $(^{36}Ar/^{37}Ar)_{Ca}$, and 4.782×10^{-3} for $(^{40}Ar/^{39}Ar)_{K}$. The uncertainty for each apparent age is given at 2σ. The argon isotope data were calculated and plotted using Isoplot 3.0 (Ludwig 2003).

Sulfur and lead isotopes

Seventeen sulfide separates and four polished thin sections from different stages of the Alastuo gold deposit were prepared for conventional and in situ sulfur isotopic analysis (ESM 2). Pyrite separates were hand-picked under the microscope to at least 99% purity. Conventional sulfur isotope analysis was carried out in the Beijing Research Institute of Uranium Geology (BRIUG) and the sulfur isotope values are reported in per mil relative to V-CDT standards with an analytical uncertainty (1σ) of ±0.2‰ for δ^{34} S. High precision in situ sulfur isotope analyses were conducted at the State Key Laboratory of Geological Processes and Mineral Resources (GPMR), China University of Geosciences, Wuhan, following the method of Zhu et al. (2017). The analyses were carried out with a Nu Plasma II MC-ICP-MS equipped with a Resonetics-S155 excimer ArF laser ablation system. The ablation protocol employed a spot diameter of 33 μm, a repetition rate of 8 Hz, and an energy fluency of about 3.5 J/cm^2. An in-house pyrite standard named WS-1 was used to calibrate the mass bias for the S isotope data (Zhu et al. 2017). The analytical precision is evaluated to be better than 0.5‰ for δ^{34} S (1σ).

Pyrite samples and whole rock samples of unaltered Precambrian biotite schist, as the dominant country rock, were analyzed for lead isotopes at the BRIUG using an ISOPROBE-T thermal ionization mass spectrometer. Lead was separated through anion exchange columns set in HBr following sample digestion. The separated lead was then loaded onto single rhenium filaments using the silica gel-phosphoric acid method. All isotopic ratios were normalized for fractionation using replicate analyses of NBS981. Estimated precision for the $^{206}Pb/^{204}Pb$, $^{207}Pb/^{204}Pb$, and $^{208}Pb/^{204}Pb$ ratios are within 0.008, 0.008, and 0.019 at the 2σ level, respectively.

EMPA analysis of chlorite

Chlorite from the main mineralization stage (stage III) was selected for electron microprobe analysis (EMPA) (Fig. 4d, e). Despite being an empirical thermometer, and therefore not fully quantitative, chlorite geothermometry can be used to estimate the temperature of mineralization (e.g.,

Cathelineau 1988). The analyses were performed using a JEOL JXA-8230 electron microprobe at the Center for Global Tectonics, School of Earth Sciences, CUG. The operating conditions were described by Ning et al. (2019) and Wang et al. (2019) in detail. A 15 kV accelerating voltage, a 20 nA probe current, and a 5-μm beam diameter were used. The following standards were used: sanidine (K), pyrope garnet (Fe, Al), diopside (Ca, Mg), jadeite (Na), rhodonite (Mn), olivine (Si), and rutile (Ti).

Results

Re-Os pyrite dating

The concentrations of Re and Os and their isotopic compositions of the pyrite samples from the Alastuo deposit are listed in ESM 4. Uncertainties, which may have resulted from errors associated with the ^{185}Re and ^{190}Os spike calibrations, weighing of samples and spikes, mass spectrometric measurement of isotopic ratios, and the ^{187}Re decay constant (Du et al. 2012) are reported as 2σ. The concentrations of the total Re and common Os in the pyrite range from 0.359 to 1.624 ng/g and 0.001 to 0.161 ng/g (ESM 4), respectively. Regression analysis of 10 samples was performed using the online ISOPLOTR program (Vermeesch 2018), yielding an isochron age of 325.8 ± 1.5 Ma on the ^{187}Re/^{188}Os vs. ^{187}Os/^{188}Os plot with an initial ^{187}Os/^{188}Os ratio (Os_i) of 0.76 ± 0.03 (Fig. 6a). The isochron has an MSWD (mean square of weighted deviates) of 60 at 2σ level of uncertainty (Fig. 6a), which indicates that the scatter is greater than what can be explained by analytical uncertainty alone. We evaluated the sensitivity of the age calculation to the scatter by removing three samples that are more deviated from the isochron line than the other seven points, which resulted in a well-defined isochron with an age of 323.8 ± 1.5 Ma, an initial ^{187}Os/^{188}Os ratio of 0.78 ± 0.03, and an MSWD of 9.2 (Fig. 6b). The two results are within uncertainty, thus providing confidence that the age of 325 ± 3 Ma and initial ^{187}Os/^{188}Os ratio of 0.7 ± 0.1 are robust.

Sericite ^{40}Ar/^{39}Ar age

The ^{40}Ar/^{39}Ar data of two sericite samples from the main mineralization stage are tabulated in ESM 5, and the apparent age spectra are illustrated in Fig. 7. Both samples yielded a consistent but somewhat perturbed age spectra with plateau or plateau-like ages of 321.7 ± 3.0 Ma and 321.2 ± 2.8 Ma, which consist of four or more consecutive steps that encompass close to 50% of the total ^{39}Ar released at the 95% confidence level (2σ).

Sulfur and lead isotopes

The results of 33 sulfur isotope analyses on pyrite, galena, and sphalerite from different paragenetic stages, analyzed with conventional and in situ analytical methods, are listed in ESM 6. Ten pyrite samples from stage II sulfide-quartz veins have a uniform range of S isotopes, with $\delta^{34}S_{V\text{-}CDT}$ values of + 5.4 ± 0.3‰ (Fig. 8a). Eighteen pyrite, three galena and two sphalerite samples from altered-rock ores of stage III have a relatively large range of $\delta^{34}S_{V\text{-}CDT}$ compositions from + 1.9 to

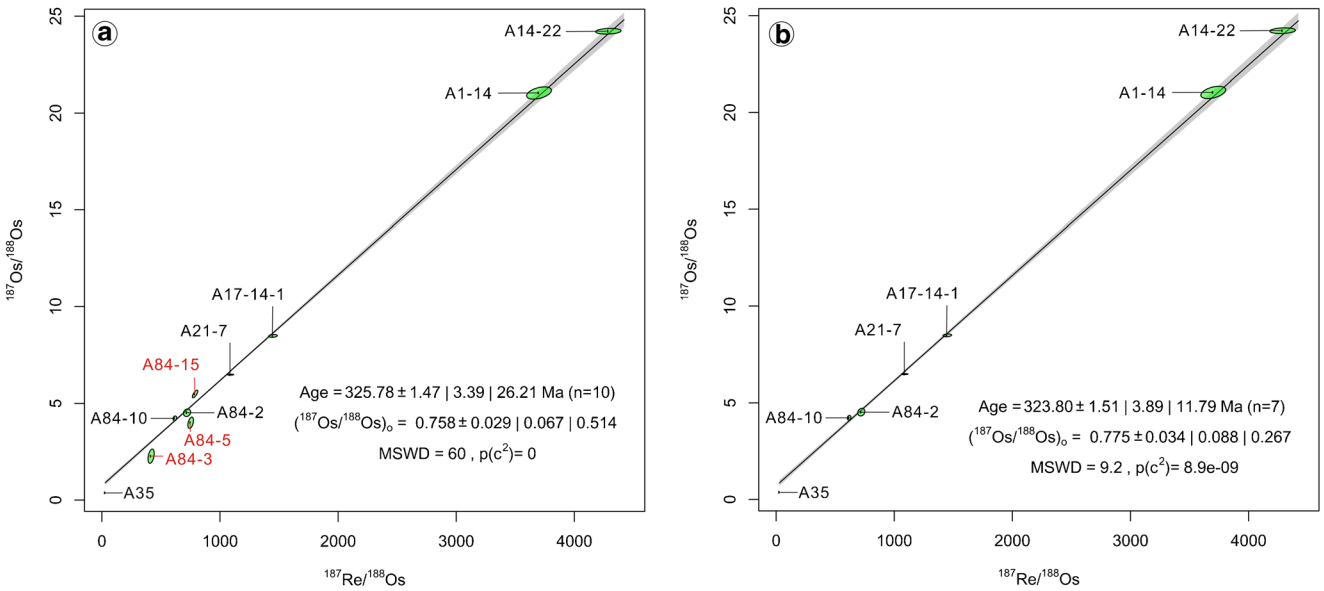

Fig. 6 Re-Os isochron diagrams for the pyrite samples from the Alastuo gold deposit. (**a**) 10-point isochron; (**b**) 7-point isochron after removing the three points that deviate from the isochron. The isochron age was generated by the ISOPLOTR software after Vermeesch (2018)

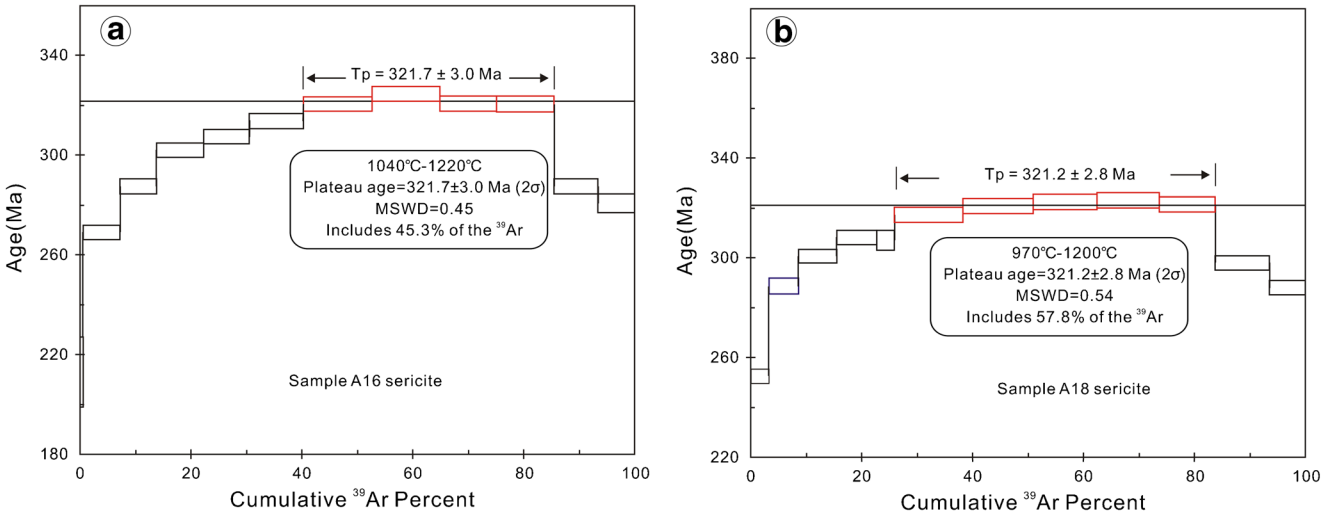

Fig. 7 $^{40}Ar/^{39}Ar$ age spectra for two sericite samples from the Alastuo gold deposit

+ 7.8‰, with a mean of + 4.6‰ (ESM 6). Plotted on Fig. 8b are the sulfur isotope ranges for MORB, OIB, subarc mantle wedge, and lithospheric continental mantle as well as those for Precambrian metamorphic rocks, Paleozoic sedimentary rocks, granitoid intrusions, and diabase dykes from the Chinese Middle Tianshan as well as other gold deposits in the Tianshan gold belt for further comparison (Zhang et al. 2018). The $\delta^{34}S_{V\text{-}CDT}$ values of the Alastuo samples overlap with, but are generally lower, than those from the Kateba'su deposit (Fig. 8b).

The lead isotope values of 14 pyrite samples from ores and 6 unaltered Precambrian biotite schist samples are listed in ESM 6 and plotted in Fig. 9, together with Pb isotope values for Carboniferous granitoids, Silurian basalts of the Bayinbuluke Formation, and pyrite from the Kateba'su gold deposit (Zhang et al. 2015; Li 2016). Lead isotope values of unaltered Precambrian biotite schist have $^{206}Pb/^{204}Pb$ ratios ranging from 18.935 to 19.232, $^{207}Pb/^{204}Pb$ from 15.629 to 15.675, and $^{208}Pb/^{204}Pb$ from 38.825 to 39.189 (ESM 6). The lead isotopes of pyrite from the altered-rock and vein-type gold ores are nearly identical with narrow ranges of $^{206}Pb/^{204}Pb$ values from 17.897 to 18.723, of $^{207}Pb/^{204}Pb$ from 15.474 to 15.643, and of $^{208}Pb/^{204}Pb$ from 37.522 to 38.299. In the $^{206}Pb/^{204}Pb$ vs. $^{207}Pb/^{204}Pb$ and $^{206}Pb/^{204}Pb$ vs. $^{207}Pb/^{204}Pb$ diagrams, the pyrite samples fall in an area that straddles the lead isotope evolution curves of the orogene and they are different from the Precambrian biotite schist samples (Fig. 9). The Pb isotopes of the pyrite samples from the Alastuo deposit overlap, but are generally more enriched in ^{207}Pb and ^{208}Pb, than those from the Kateba'su deposit (Fig. 9).

Chlorite geothermometry

Twenty EMPA analyses of chlorite from high-grade Au mineralization veins of stage III (Fig. 4d, e) yield consistent compositions with SiO_2 = 26.5–27.3 wt%, Al_2O_3 = 17.2–20.4 wt%, FeO = 21.0–23.2 wt%, MgO = 16.2–17.4 wt%, and Fe/(Fe + Mg) = 0.40–0.44 (ESM 8). The ($Na_2O + K_2O + CaO$) contents are all far lower than 0.5 wt%, indicating negligible contamination by other phyllosilicate minerals. The data were used to calculate the chemical formula of the chlorite on the basis of 14 oxygen atoms per formula unit (a.p.f.u), and the results fall mainly in the brunsvigite field (Fig. 10a). The negative correlations between Si and Al (Fig. 10b), and Fe and Mg (Fig. 10d), and the positive correlation between Si and Mg (Fig. 10c) indicate that the replacement of Si by $Al^{(IV)}$ was accompanied by the substitution of Mg by Fe. Two different empirical equations for temperature calculation, based on the tetrahedral Al content and the amount of octahedral vacancy, from Cathelineau (1988) and Jowett (1991), yielded similar temperatures ranging from 280 to 330 °C with an average of ~ 305 °C (ESM 8).

Discussion

Timing of gold mineralization and its tectonic setting

As the mineralization temperatures estimated from the chlorite geothermometry (280 to 330 °C) are significantly lower than the closure temperature of the Re-Os pyrite geochronometer (~ 500 °C; Brenan et al. 2000) and the $^{40}Ar/^{39}Ar$ sericite geochronometer (300–350 °C; McDougall and Harrison 1999), the Re-Os, and Ar-Ar ages may be used to estimate the mineralization age. Thus, based on the Re-Os ages of 325 ± 3 Ma for auriferous pyrite from stage II and $^{40}Ar/^{39}Ar$ ages of 321.7 ± 3.0 Ma and 321.2 ± 2.8 Ma (Fig. 7) for sericite from stage III, the gold mineralization at Alastuo is constrained to ~

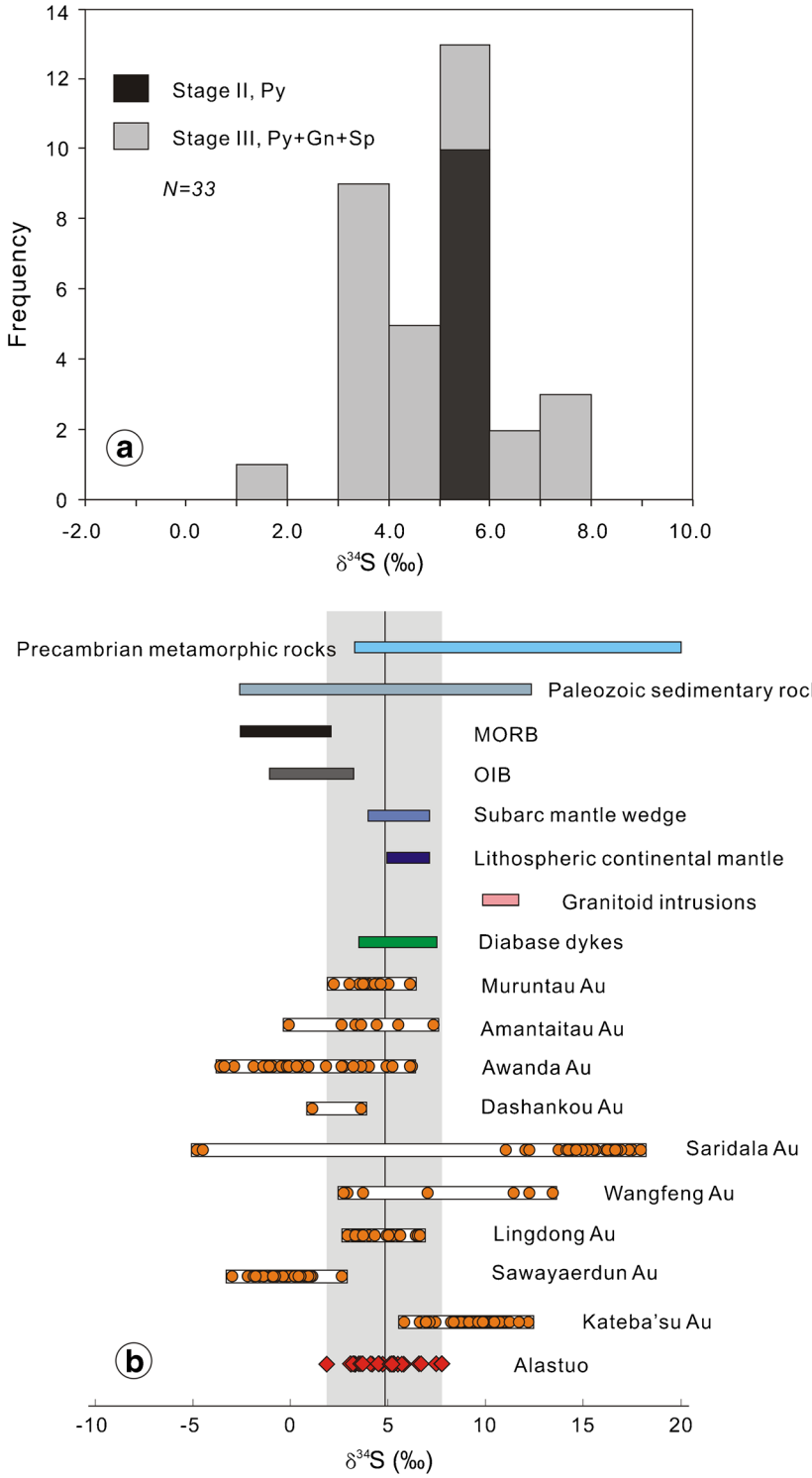

Fig. 8 (**a**) Histogram of the sulfur isotopic compositions of pyrite from the Alastuo gold deposit and their comparison with different reservoirs; (**b**) The ranges of the sulfur composition are from (Seal 2006) for MORB and OIB, from Ionov et al. (1992) for subduction-metasomatized continental lithospheric mantle of Central Asia, and from De Hoog et al. (2001) for the subarc mantle wedge. The sulfur isotopic compositions of the diabase dyke, granite rocks, Precambrian metamorphic rocks, and Hercynian sedimentary rocks of the Chinese Tianshan are from Zhang et al. (2018) and those of the gold deposits in the Tianshan are compiled from Chen et al. (2000; 2012a), Wang et al. (2001), Liu et al. (2007), Pasava et al. (2013), Ding et al. (2014), Zhang et al. (2015), Li (2016), Wang et al. (2016), Zhang et al. (2016, 2018)

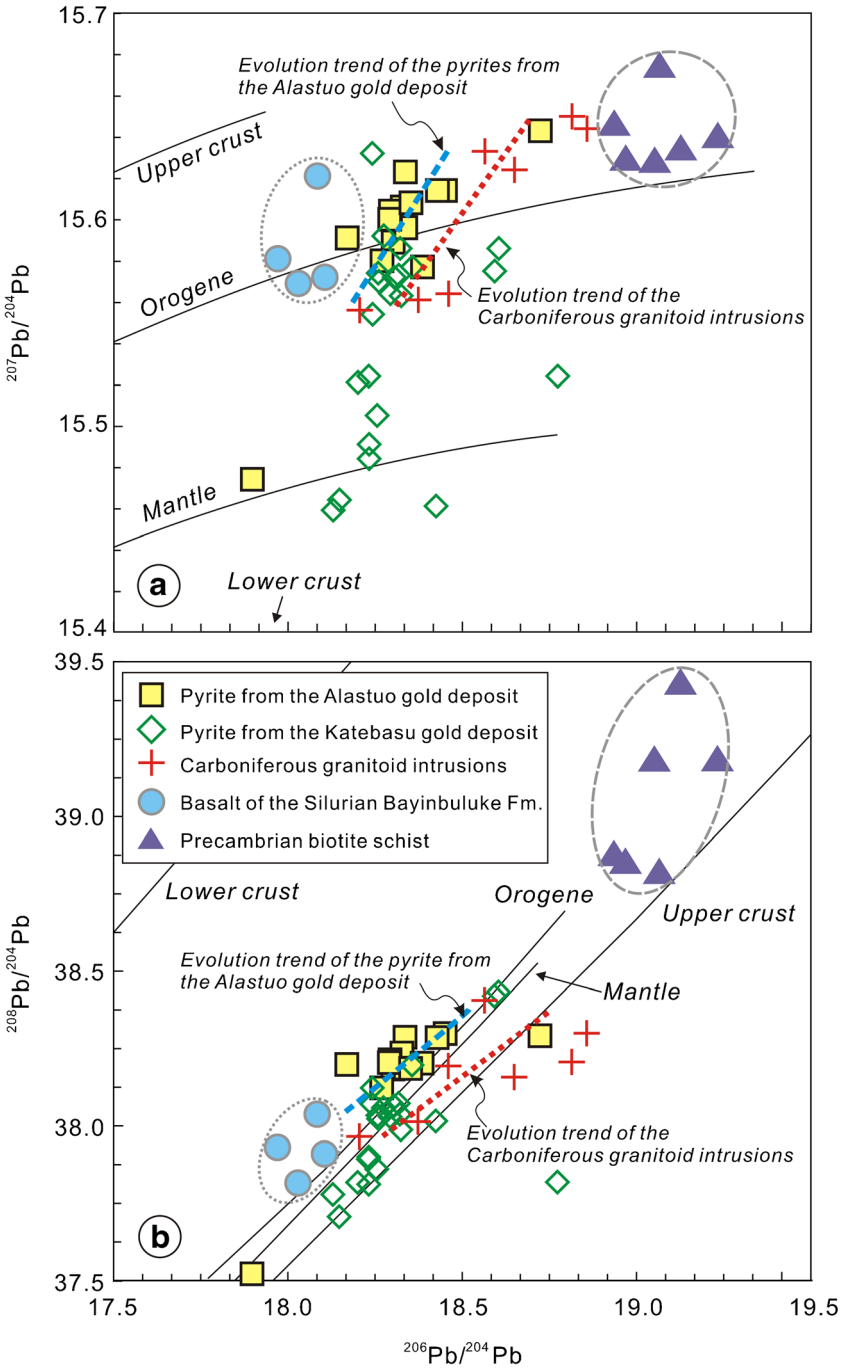

Fig. 9 $^{207}Pb/^{204}Pb$ vs. $^{206}Pb/^{204}Pb$ (**a**) and $^{208}Pb/^{204}Pb$ vs. $^{206}Pb/^{204}Pb$ diagrams (**b**) of the samples from the Alastuo gold deposit. Lead isotopes of pyrite from the Kateba'su gold deposit and of Carboniferous granitoid intrusions are from Zhang et al. (2015) and Li (2016)

325 to 320 Ma. The slightly younger sericite $^{40}Ar/^{39}Ar$ ages than the pyrite Re-Os age may be due to a combination of several factors, including the relative timing of sericite (stage III) and pyrite (stage II), the relatively low closure temperature of the $^{40}Ar/^{39}Ar$ system, and some analytical uncertainties of the two different methods. Nevertheless, the general consistency of the two sets of age data provides convincing evidence that the Alastuo deposit was formed at ~ 325 to 320 Ma, significantly postdating the host granodiorite (350.3 ± 3.0 Ma; Han et al. 2018).

The Au mineralization ages obtained in this study for Alastuo are consistent with the Rb-Sr and Re-Os isochron ages of pyrite from the Kateba'su gold deposit, which are 322.5 ± 6.8 Ma and 310.9 ± 4.2 Ma, respectively (Dong et al. 2018; Zhang et al. 2015). This indicates that the main gold mineralization epoch in the Narati region took place synchronously in the 325 to 310 Ma interval. This age interval is older than most of the orogenic gold deposits in the South Tianshan (ca. 300 to 280 Ma) that were formed in a post-collisional setting (e.g., Mao et al.

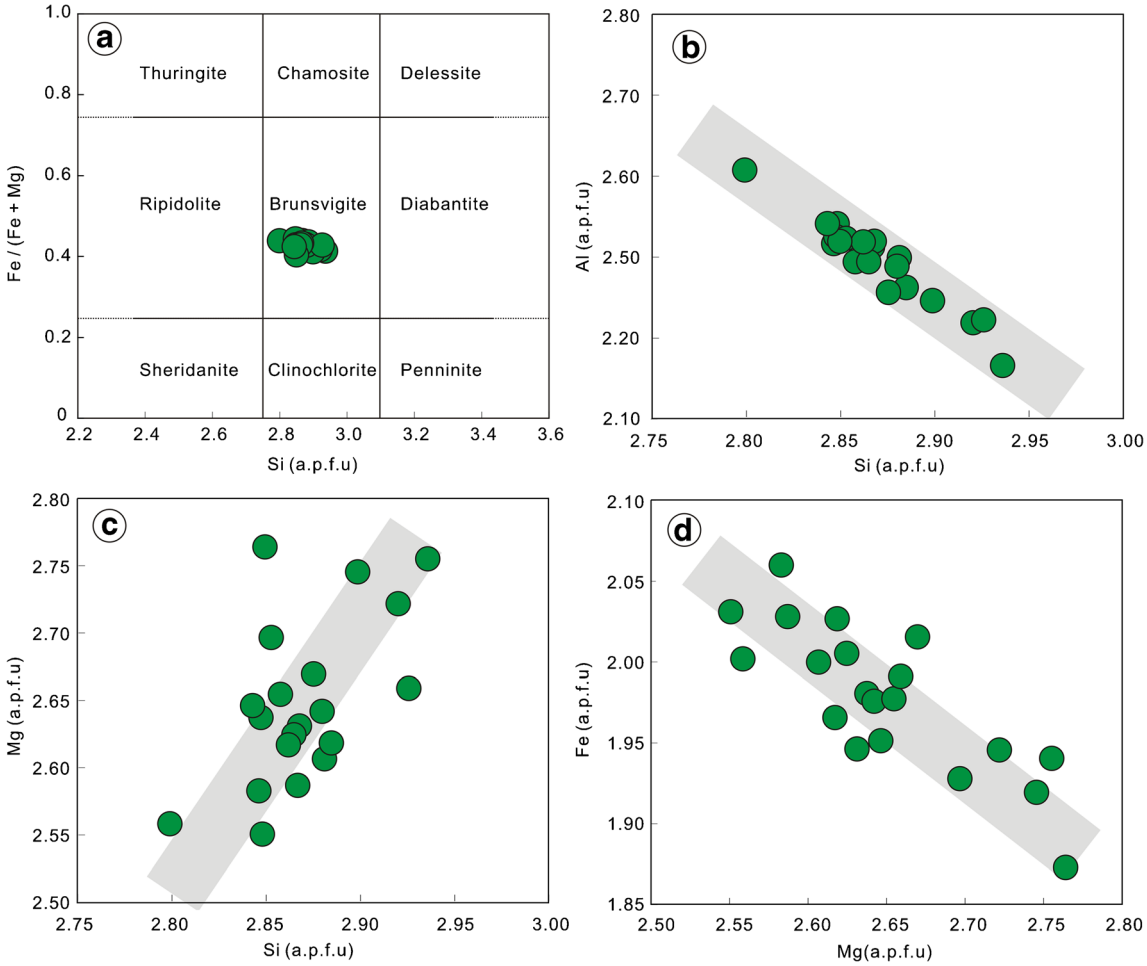

Fig. 10 (**a**) Chlorite classification diagram after Hey (1954). (**b**–**d**) Binary diagrams of major elements of chlorite in the Alastuo gold deposit

2004; Kempe et al. 2016). Rather, the gold mineralization in the Narati region is coeval with the peak high- and ultrahigh-pressure metamorphism events along the southern margins of the Middle Tianshan at Atbashi and Akeyazi (~ 326–310 Ma; Hegner et al. 2010; Gao et al. 2011; Zhang et al. 2013; Klemd et al. 2015), and with the continental collision between the Tarim craton and the Middle Tianshan (~ 325 to 310 Ma; Gao et al. 2011; Long et al. 2011; Wang et al. 2018). Taking into consideration the ca. 321 Ma age for the final closure of the South Tianshan Ocean based on dating of ophiolitic mélange (Jiang et al. 2014; Wang et al. 2018), the > 320 Ma age for subduction-related magmatic rocks (Long et al. 2011), and the zircon εHf signature indicating final consumption of the South Tianshan oceanic lithosphere at ca. 310 Ma (Han et al. 2016), the gold mineralization in the Narati region is inferred to have taken place in a transitional regime from subduction to the syn-collisional orogenic stage (Zhang et al. 2015; Wu et al. 2017; Dong et al. 2018; Zhang et al. 2018). A similar scenario can be found at Kyzylalma (Chatkal-Kurama range, Uzbekistan) that is a granite-hosted orogenic gold deposit of the same age (~ 315 Ma) as the adjacent subduction-related Kalmakyr porphyry Cu-Au deposit (Seltmann et al. 2014).

Sources of metals and fluids

Since Os and Au are both noble metals believed to be soluble in similar types of aqueous solutions (e.g., Mathur et al. 2000), the source of Os as inferred from the initial Os_i values may be used as a proxy for the source of the metals in gold deposits. The high initial $^{187}Os/^{188}Os$ ratios of 0.7 ± 0.1 estimated from the Re-Os isochron, which is significantly higher than that of a mantle reservoir (~ 0.125; Meisel et al. 2001) and lower than that of an upper crustal reservoir (> 1.0 to 1.4; Saal et al. 1998), indicates that the Os, and by inference the Au, was sourced from a mixed mantle and crustal source dominated by the crustal component (Fig. 6). Similarly, the Pb isotopes of pyrite from the Alastuo and Kateba'su gold deposits are located between the values of the supracrustal

biotite schists and mantle-derived basalts (Fig. 9), further supporting a mixed mantle and crustal source for the metals. The broad range of $\delta^{34}S$ for sulfides (+ 1.9 to + 7.8‰) from the Alastuo deposit, which resembles the range of the Muruntau (+ 2.2 to + 6.1‰; Zhang et al. 2016), Amantaitau (− 0.1 to + 7.3‰; Pasava et al. 2013) and other orogenic gold deposits in the Tianshan (Fig. 8b) and worldwide (0 to + 10‰; Goldfarb and Groves. 2015), infers a contribution of sulfur from marine sedimentary rocks (Liu et al. 2007; Chen et al. 2012a; Zhang et al. 2018), even though a magmatic source cannot be eliminated (Fig. 8a).

Specifically, in the Alastuo deposit, the granodiorite host rocks and Precambrian biotite schist are incapable of providing the metal and sulfur sources as shown by the contrasting lead isotope signatures (Fig. 9) and the apparent timing discrepancy between the gold mineralization, magmatic emplacement, and regional metamorphism. The volcano-sedimentary rocks of the Silurian Bayinbuluke Formation are undeformed and unmetamorphosed and have a limited distribution, rendering their massive devolatilization and subsequent efficient accumulation of auriferous fluid to be unrealistic, even though a similar REE pattern with the pyrite from Kateba'su deposit has been reported (Zhang et al. 2015). Thus, a subcrustal source involving the metamorphic devolatilization of a subducting oceanic slab and overlying sedimentary rocks (Goldfarb and Groves 2015; Groves et al. 2019), which could liberate sulfur and gold during the transformation of pyrite to pyrrhotite at about 500 °C (Phillips and Powell 2010), is proposed here to serve as the metal and sulfur source of the Alastuo gold deposit. This model is consistent with computer-based modeling of fluids released from a subduction zone and it satisfies the mixed metal and sulfur source required for the Alastuo deposit (e.g., Chen et al. 2004; Groves et al. 2019). Nevertheless, contributions of metals and sulfur from other sources, including the mantle wedge above the subduction zone and various crustal sources along the paths of the fluids, cannot be discounted.

Genetic model and implications for regional metallogeny

The Alastuo gold deposit has characteristics disparate with classic porphyry systems (e.g., Sillitoe 2010), including the apparent time gap (~ 25 Ma) between the emplacement of the magmatic host intrusion and the gold mineralization, the absence of intense potassic alteration, the lack of typical alteration zonation around the host intrusion, and the gold-only mineralization without an economic grade of Cu. Even though the age of Au mineralization is similar with that of the porphyry-skarn Cu-Au mineralization in west Kyrgyzstan (~ 325 to 305 Ma; Seltmann et al. 2011; Zu et al. 2019), a distinctly different tectonic evolution history in that area, as was proposed from the rather younger HP metamorphic event and ocean closure in the western part of the Talas-Fergana Fault (TFF) (~ 300 Ma; Loury et al. 2016), precludes a direct comparison in terms of mineralization types simply based on mineralization age. To date, no late Paleozoic arc volcanic rocks and related porphyry deposits have been identified in the eastern part of the Talas-Fergana Fault (TFF) (Fig. 1b).

In contrast, the mineralization styles, structural controls, metal and sulfur sources, and timing of gold mineralization at Alastuo with respect to the orogenic event are consistent with an orogenic style of gold mineralization worldwide (e.g., Groves et al. 1998, 2018, 2019; Goldfarb et al. 2005; Goldfarb and Groves 2015). The transitional tectonic setting from subduction to syn-collisional orogenic setting is consistent with typical orogenic-type gold deposits occurring at convergent plate margins, such as in the Cordilleran orogeny (Goldfarb et al. 2008). The deep-seated North Narati Fault has been regarded as the fossil suture of the Terskey Ocean (Konopelko et al. 2008), which was reactivated as a lithosphere-scale shear zone during the Late Paleozoic (Biske et al. 2013; Xue et al. 2014); and it probably accommodated much of the crustal shortening in a contractional deformation regime (Cole et al. 2000). This major regional fault may have provided foci for deformation and conduits for transcrustal fluid migration during the change in the regional stress field (Goldfarb et al. 2005). Comparable structures are associated with the emplacement of similar orogenic gold deposits worldwide (e.g., Groves et al. 2018). It is likely that the competency contrast between the granodiorite and ductile wallrocks led to increased fracturing and permeability, which focused the gold-bearing fluids into the faults within the competent granodiorite in Alastuo and in other granitoid-hosted gold deposits in Tianshan, such as Zarmitan, Jilau, Kateba'su, and Saridala (Cole et al. 2000; Abzalov 2007; Zhang et al. 2015, 2018). Interactions between auriferous fluids and iron-bearing minerals in the wallrocks, such as amphibole and biotite, to form pyrite and other sulfides would decrease the solubility of $Au(HS)_2^-$ and lead to gold deposition (Pokrovski et al. 2014; Pearce et al. 2015). The geometry, occurrence and alteration of the orebodies in the Alastuo deposit are controlled by a series of subparallel subsidiary faults in the granodiorite (Fig. 2) and emplacement of the gold deposits occurred during the transformation period from ductile shearing to brittle deformation. Collectively, all the key parameters for gold mineralization suggest that the Alastuo gold deposit represents a granitoid-hosted orogenic deposit.

The orogenic gold mineralization in the Narati region (~ 325–310 Ma) is apparently older than most of the orogenic gold deposits in the South Tianshan (~ 300–280 Ma; e.g., Mao et al. 2004). The orogenic gold deposits in the South Tianshan were generally formed in a post-collisional setting in Early Permian (Yakubchuk et al. 2005), whereas the gold mineralization in the Narati region was formed during the transitional period from a subduction to a syn-collision setting in Carboniferous. The critical trigger for the development of the orogenic gold deposits in the Tianshan could be the change of stress fields and the associated transpressive tectonics both in the subduction and collisional settings (Goldfarb et al. 2008). Similar situations can be found in the Cordilleran orogeny where orogenic gold deposits were formed during several critical episodes in the evolution of the orogeny (Goldfarb et al. 2008). Thus, it is possible to have multiple orogenic gold mineralization events within an orogenic cycle.

This study has revealed a new metallogenic event in West Tianshan, which previously has not been well-defined. The recognition of a Carboniferous orogenic gold mineralization episode calls for a reassessment of the metallogenic potential of the Narati region, especially in the Middle Tianshan along the abyssal North Narati Fault. The possibility of coeval orogenic gold mineralization events in other parts of the Tianshan Orogen also warrants further examination.

Conclusions

The Alastuo gold deposit is hosted by a granodiorite intrusion and the orebodies are controlled by a series of subsidiary faults of the transcrustal North Narati Fault. Gold mineralization occurs dominantly as dissemination in altered rocks, to a lesser extent as veins, and is closely associated with alteration minerals including quartz, chlorite, epidote, pyrite, and galena. The mineralization took place during the second and third stages that are characterized by tectonic transformation from ductile shearing to brittle deformation, with temperatures from 280 to 330 °C, as indicated by chlorite geothermometry.

A robust gold mineralization age of ~ 325 to 320 Ma is revealed for Alastuo from consistent pyrite Re-Os isochron and sericite $^{40}Ar/^{39}Ar$ plateau-like ages, which are much younger than the host granodiorite (ca. 350 Ma) and constrain the gold mineralization in the Narati region in a 325 to 310 Ma interval. This time interval corresponds to a transitional regime from subduction to continental collision between the Tarim block and Middle Tianshan terrane.

The initial Os_i value of 0.7 ± 0.1 estimated from Re-Os isochron of pyrite, the Pb isotopes of pyrite and the sulfur isotopes of the sulfides ($\delta^{34}S_{V\text{-}CDT}$ = + 1.9 to + 7.8‰) suggest that the metals and sulfur may have been derived from mixed mantle and crustal sources, through processes including metamorphic devolatilization of a subducting oceanic slab and its overlying sedimentary rocks.

The mineralization styles, structural controls, metal and sulfur sources, and timing of the gold mineralization with respect to the orogenic event suggest that the Alastuo gold deposit represents an orogenic type gold mineralization. This newly recognized Carboniferous orogenic mineralization event calls for a re-evaluation of the gold metallogeny in the Middle Tianshan along North Narati Fault.

Acknowledgments We would like to thank Haijun Ma, Jianhua Han, Xinfang Xu, and Weizhong Yang from the First Brigade of the Regional Geological Survey of the Xinjiang Bureau of Geology and Mineral Resources for access to the Alastuo gold deposit. Drs. Kuidong Zhao, Wen Chen, Junpeng Wang, and Shuiyuan Yang were particularly helpful with sample analyses. We are grateful to Drs. David T A Symons, Xiaobo Zhao, Liang Zhang, Yun Zhao, Hao Xing, Guozhen Zhang, and Bing Xiao for the fruitful discussions and assistance during the drafting of this paper. Constructive and helpful comments from Dr. Bernd Lehmann, Huayong Chen, Yanjing Chen, and another anonymous reviewer have remarkably improved the quality of this paper. This work was supported by National Key Research and Development Program of China (2017YFC0601202), Strategic Priority Research Program of the Chinese Academy of Sciences (XDA20070304), National Science Foundation of China (41802108), and Fundamental Research Funds for the Central Universities (CUGL170812). This article is a contribution to the IGCP-662 project that is co-sponsored by IUGS and UNESCO.

References

Abzalov M (2007) Zarmitan granitoid-hosted gold deposit, Tian Shan belt, Uzbekistan. Econ Geol 102:519–532

Alexeiev DV, Kröner A, Hegner E, Rojas-Agramonte Y, Biske YS, Wong J, Geng HY, Ivleva EA, Mühlberg M, Mikolaichuk AV, Liu D (2016) Middle to Late Ordovician arc system in the Kyrgyz Middle Tianshan: from arc-continent collision to subsequent evolution of a Palaeozoic continental margin. Gondwana Res 39:261–291

Bahebatuo Mining Company (2015) Geologic survey report of the Alastuo gold deposit area in Xinjiang, China, pp 118

Biske YS, Konopelko DL, Seltmann R (2013) Geodynamics of late Paleozoic magmatism in the Tien Shan and its framework. Geotectonics 47:291–309

Brenan JM, Cherniak DJ, Rose LA (2000) Diffusion of osmium in pyrrhotite and pyrite: implications for closure of the Re-Os isotopic system. Earth Planet Sci Lett 180:399–413

Cathelineau M (1988) Cation site occupancy in chlorites and illites as a function of temperature. Clay Miner 23:471–485

Charvet J, Shu L, Laurent-Charvet S, Wang B, Faure M, Cluzel D, Chen Y, De Jong K (2011) Palaeozoic tectonic evolution of the Tianshan belt, NW China. Sci China Earth Sci 54:166–184

Chen Y (2000) Progress in the study of Central Asia-type orogenesis-metallogenesis in Northwest China. Geol J of China Univ 6:17–22

Chen H, Bao J, Zhang Z, Liu Y, Ni P, Ling H (2000) Isotopic indication to source of ore materials and fluids of the Wangfeng gold deposit in Tianshan: a case study of metallogenesis during collisional orogenesis. Sci China Ser D Earth Sci 43:156–166

Chen W, Liu X, Zhang S (2002) Continuous laser stepwise heating 40Ar/39Ar dating technique. Geol Rev 48:127–134

Chen Y, Pirajno F, Sui Y (2004) Isotope geochemistry of the Tieluping silver-lead deposit, Henan, China: a case study of orogenic silver-dominated deposits and related tectonic setting. Mineral Deposita 39:560–575

Chen Y, Liu D, Tang Y, Wang D, Dong L, Xu X, Wang X (2008) Mineral resources and mineralization system in Tianshan, China. Geological Publishing House, Beijing, p 1063

Chen H, Chen Y, Baker M (2012a) Isotopic geochemistry of the Sawayaerdun orogenic-type gold deposit, Tianshan, northwest China: implications for ore genesis and mineral exploration. Chem Geol 310-311:1–11

Chen Y, Pirajno F, Wu G, Qi JP, Xiong XL (2012b) Epithermal deposits in North Xinjiang, NW China. Int J Earth Sci 101:889–917

Chen H, Wan B, Pirajno F, Chen Y, Xiao B (2018) Metallogenesis of the Xinjiang Orogens, NW China - new discoveries and ore genesis. Ore Geol Rev 100:1–11

Cole A, Wilkinson JJ, Halls C, Serenko TJ (2000) Geological characteristics, tectonic setting and preliminary interpretations of the Jilau gold-quartz vein deposit, Tajikistan. Mineral Deposita 35:600–618

De Hoog J, Mason P, van Bergen MM (2001) Sulfur and chalcophile elements in subduction zones: constraints from a laser ablation ICP-MS study of melt inclusions from Galunggung Volcano, Indonesia. Geochim Cosmochim Acta 65:3147–3164

Ding QF, Wu CZ, Santosh M, Fu Y, Dong LH, Qu X, Gu LX (2014) H-O, S and Pb isotope geochemistry of the Awanda gold deposit in southern Tianshan, central Asian orogenic belt: implications for fluid regime and metallogeny. Ore Geol Rev 62:40–53

Dolgopolova A, Seltmann R, Konopelko D, Biske YS, Shatov V, Armstrong R, Belousova E, Pankhurst R, Koneev R, Divaev F (2017) Geodynamic evolution of the western Tien Shan, Uzbekistan: insights from U-Pb SHRIMP geochronology and Sr-Nd-Pb-Hf isotope mapping of granitoids. Gondwana Res 47:76–109

Dong L, Wan B, Yang W, Deng C, Chen Z, Yang L, Cai K, Xiao W (2018) Rb-Sr geochronology of single gold-bearing pyrite grains from the Katbasu gold deposit in the South Tianshan, China and its geological significance. Ore Geol Rev 100:99–110

Du A, Qu W, Wang D, Li C (2012) Re-Os dating and its application in deposits. Geological Publishing House, Beijing, p 182

Gao J, Long L, Klemd R, Qian Q, Liu D, Xiong X, Su W, Liu W, Wang Y, Yang F (2009) Tectonic evolution of the South Tianshan orogen and adjacent regions, NW China: geochemical and age constraints of granitoid rocks. Int J Earth Sci 98:1221–1238

Gao J, Klemd R, Qian Q, Zhang X, Li J, Jiang T, Yang Y (2011) The collision between the Yili and Tarim blocks of the southwestern Altaids: geochemical and age constraints of a leucogranite dike crosscutting the HP-LT metamorphic belt in the Chinese Tianshan Orogen. Tectonophys 499:118–131

Gao Y, Zhang Z, Wang Z, Yang W, Ban J, Dong F, Tan W (2015) Geochronology of the Katabaasu gold deposit in West Tian Shan and its geological significance: evidence from ^{40}Ar–^{39}Ar isotopic ages of sericite. Geol Explor 51:805–815

Goldfarb RJ, Groves DI (2015) Orogenic gold: common or evolving fluid and metal sources through time. Lithos 233:2–26

Goldfarb RJ, Groves DI, Hart CJR, Baker T, Dubé B, Gosselin P (2005) Distribution, character, and genesis of gold deposits in metamorphic terranes. Econ Geol 100th Anniv 100:407–450

Goldfarb RJ, Hart CJ, Marsh EE (2008) Orogenic gold and evolution of the cordilleran orogen. Ores and orogenesis: circum-Pacific tectonics, geologic evolution, and ore deposits. Arizona Geol Soc Digest 22:311–323

Groves DI, Goldfarb RJ, Gebre-Mariam M, Hagemann SG, Robert F (1998) Orogenic gold deposits: a proposed classification in the context of their crustal distribution and relationship to other gold deposit types. Ore Geol Rev 13:7–27

Groves DI, Santosh M, Goldfarb RJ, Zhang L (2018) Structural geometry of orogenic gold deposits: implications for exploration of world-class and giant deposits. Geosci Front 9:1163–1177

Groves DI, Santosh M, Deng J, Wang Q, Yang L, Zhang L (2019) A holistic model for the origin of orogenic gold deposits and its implications for exploration. Mineral Deposita. https://doi.org/10.1007/s00126-019-00877-5

Han Y, Zhao G, Sun M, Eizenh Fer PR, Hou W, Zhang X, Liu Q, Wang B, Liu D, Xu B (2016) Late Paleozoic subduction and collision processes during the amalgamation of the central Asian Orogenic Belt along the south Tianshan suture zone. Lithos 246-247:1–12

Han Y, Liu Y, Zhou S, Teng F, Wei J, Tian R (2018) Geochemistry and chronology of the granites in Alasituo, west Tianshan Orogen: implications for a magma mixing origin. Geol J 53:44–59

He Z, Wang B, Zhong L, Zhu X (2018) Crustal evolution of the central Tianshan block: insights from zircon U-Pb isotopic and structural data from meta-sedimentary and meta-igneous rocks along the Wulasitai - Wulanmoren shear zone. Precambrian Res 314:111–128

Hegner E, Klemd R, Kröner A, Corsini M, Alexeiev DV, Iaccheri LM, Zack T, Dulski P, Xia X, Windley BF (2010) Mineral ages and PT conditions of late Paleozoic high-pressure eclogite and provenance of mélange sediments from Atbashi in the south Tianshan orogen of Kyrgyzstan. Am J Sci 310:916–950

Hey M (1954) A new review of the chlorite. Mineral Mag 30:277–292

Huang H, Zhang Z, Santosh M, Zhang D, Wang T (2015a) Petrogenesis of the early Permian volcanic rocks in the Chinese south Tianshan: implications for crustal growth in the central Asian Orogenic Belt. Lithos 228-229:23–42

Huang Z, Long X, Kröner A, Yuan C, Wang Y, Chen B, Zhang Y (2015b) Neoproterozoic granitic gneisses in the Chinese central Tianshan block: implications for tectonic affinity and Precambrian crustal evolution. Precambrian Res 269:73–89

Ionov DA, Hoefs J, Wedepohl KH, Wiechert U (1992) Content and isotopic composition of Sulphur in ultramafic xenoliths from Central Asia. Earth Planet Sci Lett 111:269–286

Jahn B (2004) The central Asian Orogenic Belt and growth of the continental crust in the Phanerozoic. Geol Soc Lond, Spec Publ 226:73–100

Jiang T, Gao J, Klemd R, Qian Q, Zhang X, Xiong X, Wang X, Tan Z, Chen B (2014) Paleozoic ophiolitic mélanges from the south Tianshan Orogen, NW China: geological, geochemical and geochronological implications for the geodynamic setting. Tectonophys 612-613:106–127

Jowett EC (1991) Fitting iron and magnesium into the hydrothermal chlorite geothermometer GAC/MAC/SEG Joint Annual Meeting, Toronto, May 27–29, 1991, Program with Abstracts 16

Kempe U, Graupner T, Seltmann R, de Boorder H, Dolgopolova A, Zeylmans Van Emmichoven M (2016) The Muruntau gold deposit (Uzbekistan) - a unique ancient hydrothermal system in the southern Tien Shan. Geosci Front 7:495–528

Klemd R, Gao J, Li J, Meyer M (2015) Metamorphic evolution of (ultra)-high-pressure subduction-related transient crust in the south Tianshan Orogen (central Asian Orogenic Belt): geodynamic implications. Gondwana Res 28:1–25

Konopelko D, Biske G, Seltmann R, Kiseleva M, Matukov D, Sergeev S (2008) Deciphering Caledonian events: timing and geochemistry of the Caledonian magmatic arc in the Kyrgyz Tien Shan. J Asian Earth Sci 32:131–141

Kudrin VS, Solov'Yev SG, Stavinskiy VA, Karabdin LL (1990) The gold-copper-molybdenum-tungsten ore belt of the Tien Shan. Int Geol Rev 32:930–941

Li Z (2016) Study on the geological-geochemical characteristics and origin of the Katebasu gold-copper deposit, West Tianshan, Xinjiang. Master dissertation, Chang'an University, Xi'an. pp 60

Liu J, Zheng M, Cook NJ, Long X, Deng J, Zhai Y (2007) Geological and geochemical characteristics of the Sawaya'erdun gold deposit, southwestern Chinese Tianshan. Ore Geol Rev 32:125–156

Liu Y, Han Y, Li Z, Mo X, Huang Y, Li Y (2018) Geological characteristics, deposit type, and metallogenic epoch of the Katebasu gold-copper deposit in western Tianshan. Geol J 53:263–277

Long L, Gao J, Klemd R, Beier C, Qian Q, Zhang X, Wang J, Jiang T (2011) Geochemical and geochronological studies of granitoid rocks from the Western Tianshan Orogen: implications for continental growth in the southwestern central Asian Orogenic Belt. Lithos 126:321–340

Loury C, Rolland Y, Cenki-Tok B, Lanari P, Guillot S (2016) Late Paleozoic evolution of the south Tien Shan: insights from P-T estimates and allanite geochronology on retrogressed eclogites (Chatkal range, Kyrgyzstan). J Geodyn 96:62–80

Ludwig KR (2003) User's manual for Isoplot 3.00: a geochronological toolkit for Microsoft Excel. Berkeley Geochronl Cent Spec Publ 4: 25–32

Ma X, Shu L, Meert JG, Li J (2014) The Paleozoic evolution of central Tianshan: geochemical and geochronological evidence. Gondwana Res 25:797–819

Mao J, Konopelko D, Seltmann R, Lehmann B, Chen W, Wang Y, Eklund O, Usubaliev T (2004) Postcollisional age of the Kumtor gold deposit and timing of Hercynian events in the Tien Shan, Kyrgyzstan. Econ Geol 99:1771–1780

Mathur R, Ruiz J, Titley S, Gibbins S, Margotomo W (2000) Different crustal sources for Au-rich and Au-poor ores of the Grasberg Cu-Au porphyry deposit. Earth Planet Sci Lett 183:7–14

McDougall I, Harrison TM (1999) Geochronology and thermochronology by the $^{40}Ar/^{39}Ar$ method. Oxford University Press. pp 212

Meisel T, Walker RJ, Irving AJ, Lorand J (2001) Osmium isotopic compositions of mantle xenoliths: a global perspective. Geochim Cosmochim Acta 65:1311–1323

Ning W, Wang J, Xiao D, Li F, Huang B, Fu D (2019) Electron probe microanalysis of monazite and its applications to U-Th-Pb dating of geological samples. J Earth Sci 30:952–963

Pasava J, Frimmel H, Vymazalová A, Dobes P, Jukov AV, Koneev RI (2013) A two-stage evolution model for the Amantaytau orogenic-type gold deposit in Uzbekistan. Mineral Deposita 48:825–840

Pearce MA, White AJR, Fisher LA, Hough RM, Cleverley JS (2015) Gold deposition caused by carbonation of biotite during late-stage fluid flow. Lithos 239:114–127

Phillips GN, Powell R (2010) Formation of gold deposits: a metamorphic devolatilization model. J Metamorph Geol 28:689–718

Pirajno F, Seltmann R, Yang Y (2011) A review of mineral systems and associated tectonic settings of northern Xinjiang, NW China. Geosci Front 2:157–185

Pokrovski GS, Akinfiev NN, Borisova AY, Zotov AV, Kouzmanov K (2014) Gold speciation and transport in geological fluids: insights from experiments and physical-chemical modelling. Geol Soc Lond, Spec Publ 402:9–70

Qu W, Du A, Li C, Sun W (2009) High-precise determination of osmium isotopic ratio in the Jinchuan copper-nickel sulfide ore samples. Rock & Mineral Analysis 28:219–222

Rui Z, Goldfarb RJ, Qiu Y, Zhou T, Chen R, Pirajno F, Yun G (2002) Paleozoic–early Mesozoic gold deposits of the Xinjiang autonomous region, northwestern China. Mineral Deposita 37:393–418

Saal AE, Rudnick RL, Ravizza GE, Hart SR (1998) Re-Os isotope evidence for the composition, formation and age of the lower continental crust. Nature 393:58–61

Seal RR (2006) Sulfur isotope geochemistry of sulfide minerals. Rev Mineral Geochem 61:633–677

Seltmann R, Konopelko D, Biske G, Divaev F, Sergeev S (2011) Hercynian post-collisional magmatism in the context of Paleozoic magmatic evolution of the Tien Shan orogenic belt. J Asian Earth Sci 42:821–838

Seltmann R, Porter TM, Pirajno F (2014) Geodynamics and metallogeny of the central Eurasian porphyry and related epithermal mineral systems: a review. J Asian Earth Sci 79:810–841

Sengör A, Natal'In BA, Burtman VS (1993) Evolution of the Altaid tectonic collage and Palaeozoic crustal growth in Eurasia. Nature 364:299–307

Sillitoe RH (2010) Porphyry copper systems. Econ Geol 105:3–41

Soloviev SG, Kryazhev S, Dvurechenskaya S (2018) Geology, mineralization, and fluid inclusion study of the Kuru-Tegerek Au-Cu-Mo skarn deposit in the Middle Tien Shan, Kyrgyzstan. Mineral Deposita 53:195–223

Steiger RH, Jäger E (1977) Subcommission on geochronology: convention on the use of decay constants in geo-and cosmochronology. Earth Planet Sci Lett 36:359–362

Vermeesch P (2018) IsoplotR: a free and open toolbox for geochronology. Geosci Front 9:1479–1493

Wang S (1983) Age determinations of ^{40}Ar-^{40}K, ^{40}Ar-^{39}Ar and radiogenic ^{40}Ar released characteristics on K-Ar geostandards of China. Chinese J Geol 4:315–323

Wang J, Liu Y, Zhou D, Lu G (2001) Geological features and origin of Saridala gold deposit, Xinjiang. Mineral Deposits 20:385–393

Wang B, Faure M, Cluzel D, Shu L, Charvet J, Meffre S, Ma Q (2006) Late Paleozoic tectonic evolution of the northern west Chinese Tianshan Belt. Geodin Acta 19:237–247

Wang X, Huang Y, Chen G, Gao J (2016) Geology, S-Pb-Os isotopic compositions and re-Os dating of the Lingdong gold deposit in the eastern Tien Shan. Acta Petrol Sin 32:1409–1419

Wang X, Gao J, Klemd R, Jiang T, Li J, Zhang X, Xue S (2017) The central Tianshan block: a microcontinent with a Neoarchean-Paleoproterozoic basement in the southwestern central Asian Orogenic Belt. Precambrian Res 295:130–150

Wang X, Klemd R, Gao J, Jiang T, Li J, Xue S (2018) Final assembly of the southwestern central Asian Orogenic Belt as constrained by the evolution of the south Tianshan Orogen: links with Gondwana and Pangea. J Geophys Res Solid Earth 123:7361–7388

Wang J, Li X, Ning W, Kusky T, Wang L, Polat A, Deng H (2019) Geology of a Neoarchean suture: evidence from the Zunhua ophiolitic mélange of the eastern Hebei Province, North China Craton. GSA Bulletin. https://doi.org/10.1130/B35138.1

Wu Y, Chen Y, Zhou K (2017) Mo deposits in Northwest China: geology, geochemistry, geochronology and tectonic setting. Ore Geol Rev 81: 641–671

Xiao W, Windley BF, Allen MB, Han C (2013) Paleozoic multiple accretionary and collisional tectonics of the Chinese Tianshan orogenic collage. Gondwana Res 23:1316–1341

Xiao W, Windley BF, Sun S, Li J, Huang B, Han C, Yuan C, Sun M, Chen H (2015) A tale of amalgamation of three Permo-Triassic collage systems in Central Asia: Oroclines, sutures, and terminal accretion. Annu Rev Earth Planet Sci 43:477–507

Xu X, Wang H, Li P, Chen J, Ma Z, Zhu T, Wang N, Dong Y (2013) Geochemistry and geochronology of Paleozoic intrusions in the Nalati (Narati) area in western Tianshan, Xinjiang, China: implications for Paleozoic tectonic evolution. J Asian Earth Sci 72:33–62

Xue C, Zhao X, Mo X, Dong L, Gu X, Nurtaev B, Pak N, Zhang Z, Wang X, Zu B, Zhang G, Feng B, Liu J (2014) Asian gold belt in western Tianshan and its dynamic setting, metallogenic control and exploration. Earth Sci Front 21:128–155

Yakubchuk A, Cole A, Seltmann R, Shatov V (2002) Tectonic setting, characteristics, and regional exploration criteria for gold mineralization in the Altaid orogenic collage: the Tien Shan province as a key example. Spec Publ Soc Econ Geol 9:177–202

Yakubchuk AS, Shatov VV, Kirwin D, Tomurtogoo O, Badarch G, Buryak AA (2005) Gold and base metal metallogeny of the Central Asian Orogenic supercollage. Econ Geol 100th Anniv 100:1035–1068

Yang W, Xue C, Zhao X, Zhao S, Wei J, Feng B, Zhou H, Lin Z, Zheng H, Liu J, Zhang Q, Zu B (2013) The discovery of the Kateba'asu large Au-Cu deposit in Xinyuan County, western Tianshan, Xinjiang. Geol Bull China 32:1613–1620

Zhang L, Du J, Lü Z, Yang X, Gou L, Xia B, Chen Z, Wei C, Song S (2013) A huge oceanic-type UHP metamorphic belt in southwestern Tianshan, China: peak metamorphic age and P-T path. Chin Sci Bull 58:4378–4383

Zhang Q, Xue CJ, Zhao XB, Feng B, Xing H, Mo XX, Zhao SM, Yang WZ, Xing L (2015) Geology, geochemistry and metallogenic epoch of the Katebasu large-sized gold deposit, Western Tianshan Mountains, Xinjiang. Geol China 42:411–437

Zhang G, Li Z, Dong X, Liu J (2016) Ore geology of Muruntau world-class gold deposit and S-Pb isotopic tracing. Acta Petrol Sin 32: 1333–1345

Zhang H, Zhu Y, Feng W, Tan Y, An F, Zheng J (2017) Paleozoic intrusive rocks in the Nalati mountain range (NMR), southwest Tianshan: geodynamic evolution based on petrology and geochemical studies. J Earth Sci 28:196–217

Zhang L, Chen H, Liu C, Zheng Y (2018) Ore genesis of the Saridala gold deposit, Western Tianshan, NW China: constraints from fluid inclusion, S-Pb isotopes and $^{40}Ar/^{39}Ar$ dating. Ore Geol Rev 100:63–76

Zhao W, Zhao X, Xue C, Symons DTA, Cui X, Xing L (2019) Structural characterization of the Katebasu gold deposit, Xinjiang, China: tectonic correlation with the amalgamation of the western Tianshan. Ore Geol Rev 107:888–902

Zhong L, Wang B, Alexeiev DV, Cao Y, Biske YS, Liu H, Zhai Y, Xing L (2017) Paleozoic multi-stage accretionary evolution of the SW Chinese Tianshan: new constraints from plutonic complex in the Nalati range. Gondwana Res 45:254–274

Zhu Y, Zhou J, Zeng Y (2007) The Tianger (Bingdaban) shear zone hosted gold deposit, west Tianshan, NW China: petrographic and geochemical characteristics. Ore Geol Rev 32:337–365

Zhu Z, Jiang S, Ciobanu CL, Yang T, Cook NJ (2017) Sulfur isotope fractionation in pyrite during laser ablation: implications for laser ablation multiple collector inductively coupled plasma mass spectrometry mapping. Chem Geol 450:223–234

Zu B (2016) Metallogeny and prospecting potential of gold deposits in Asia Gold Belt, Western Tianshan. Doctoral dissertation, China University of Geosciences, Beijing, pp 228

Zu B, Seltmann R, Xue C, Wang T, Dolgopolova A, Li C, Zhou L, Pak N, Ivleva E, Chai M, Zhao X (2019) Multiple episodes of Late Paleozoic Cu-Au mineralization in the Chatkal-Kurama terrane: new constraints from the Kuru-Tegerek and Bozymchak skarn deposits, Kyrgyzstan. Ore Geol Rev 113:103077. https://doi.org/10.1016/j.oregeorev.2019.103077